

# A STRUCTURAL ANALYSIS OF THE THERMAL CONDUCTIVITY OF PAPER COATINGS: APPLICATION OF PARTICLE DEPOSITION SIMULATION TO A LUMPED PARAMETER MODEL

*Philip Gerstner<sup>1</sup>, Cathy J. Ridgway<sup>2</sup>, Jouni Paltakari<sup>1</sup>  
and Patrick A. C. Gane<sup>1,2</sup>*

<sup>1</sup>Helsinki University of Technology, Faculty of Chemistry and Materials Science, Department of Forest Products Technology, Vuorimiehentie 1A, P.O. Box 6300, 02150 Espoo, Finland, email: [firstname.lastname@tkk.fi](mailto:firstname.lastname@tkk.fi)

<sup>2</sup>Omya Development AG, CH-4665 Oftringen, Switzerland, email: [firstname.lastname@omya.com](mailto:firstname.lastname@omya.com)

## ABSTRACT

Thermal conductivity of paper coating structures can be regarded as an important property for many processes involving the application of thermal energy on coated papers. This work analyses the thermal conductivity of coatings in terms of their structure. A Monte Carlo simulation-based particle deposition was used to create idealised two-dimensional coating structures. They acted as a master template for the superimposed parameters of a Lumped Parameter Model for the calculation of thermal conductivity, in which pigment and binder are treated as separate solid phases within a fluid (air). Binder alone was initially assumed to provide the necessary thermal connectivity. Comparison of the numerically calculated conductivities with corresponding experimental

results, obtained from ground calcium carbonate pigment structures, showed generally lower calculated conductivities and clear differences in the change of conductivity when increasing latex binder content. Two different mechanisms are suggested as the cause of this lack of correlation. Firstly, it is shown that both the simulation and the current Lumped Parameter Model do not account sufficiently for pigment connectivity. This is the reason for the underestimation, especially evident when no binder is present. The nature of pigment connectivity is related to polymer dispersant on the pigment surface and the surface crystallite planar structures, if present, mostly related to larger particles. Secondly, it is confirmed that surface and colloid chemistry factors cause binder to accumulate first at pigment nodal points, which causes a disruption of the pigment packing already at 6 w/w% binder. This creates inhomogeneity in the real coating structure which is not accounted for by the homogeneous assumption of the model. It could be shown that an introduced parameter of pigment connectivity becomes lower for the binder concentrations for which pigment disruption occurs. It is shown that the method is sensitive enough in respect to refinement of both pigment and latex connectivity factors to allow identification and parameterisation of the subtleties occurring in real colloiddally interactive particulate systems that are reflected in the thermal conductivity response of the dried coating structure.

**Keywords:** Porous media, particle deposition, coating structure, modelling, thermal conductivity, electrophotography, web drying, thermal calendering, heatset offset

## INTRODUCTION

Thermal conductivity of paper coating structures can be regarded as an important property in many steps of coated paper production (drying) [1], finishing (thermal calendering) [2], converting (heat sealing) and printing (electrophotography, heatset web-offset) [3] as well as in the end use properties of specially coated grades (thermal papers) and barrier films. The rising costs for energy continue to draw attention to ensuring its most effective use. Processes, as mentioned above, involving the application of thermal energy onto coated papers, may benefit from a better knowledge of the thermal

transfer in two identifiable ways. On the one hand, the flow of energy and its local effects should be better understood. This would enable optimisation of the thermal efficiency by adjusting either the process parameters or the coating structure itself. On the other hand, better knowledge of the thermal response of coatings also creates new possibilities to improve the product quality. Especially in processes where interactions of the interface of the coating layer play an important role, i.e. in printing, it is not only the coating structure itself, but also the thermal response that the structure creates, which ultimately affects the product quality.

Being multi-phase porous media, paper coatings show a complex relationship between thermal conductivity and their structural properties. The binder phase plays an important role in formation of the coating structure [4] and therefore, porosity alone is found to be insufficient in describing the thermal conductivity [5]. A generalised model, which is able to describe the relationship of pigment and binder in the coating structure, is therefore required. This work focuses on generating such a model and analyzes two-dimensional pigment/binder structures created by a simulated particle deposition for the subsequent parameterisation of a general Lumped Parameter Model for the calculation of thermal conductivity of fine pigmented porous structures. We separate the terms simulation and model: “*simulation*” being used in the sense of “the imitative representation of the functioning of one system or process by means of the functioning of another”, whereas the term “*model*” relates to “a system of postulates, data and inferences presented as a mathematical description of an entity or state of affairs” [6]. In this work, a Monte Carlo based particle deposition is used for the simulation of coating structures, while the Lumped Parameter Model is used to describe the thermal conductivity of the simulated coating structures.

In addition, the simulated particle packings are compared to real coating structures in the form of cross-sectional scanning electron microscope (SEM) images. The calculated effective thermal conductivities of the model for both simulated structures and real structures are compared to experimentally determined values. In this way, both the simulation and modelling have a practical reference, and it is possible to point out valuable structural features introduced in real systems that can be traced back to materials interactions, such as colloidal instabilities manifest in rheological properties and the dynamics of consolidation [7, 8].

## **MATERIALS AND METHODS**

### **Outline**

In this work, experimental thermal conductivities of a pigment-binder system are compared with the thermal conductivities calculated by application of a Lumped Parameter Model applied to two-dimensional simulated structures – the simulated structure acting as a master template to determine the parameters of the superposed Lumped Parameter Model unit cell. In order to compare directly experimental values with values obtained by simulation and modelling, and thus examine and correct possible shortcomings of the simulation and/or model, a separable analysis of the simulation and the model is required.

The quality of the simulation compared with reality is first investigated by replacing the 2D simulation master of the pigment-binder structure by cross-sectional SEM-images of real coating structures, in which the latex binder is distinguished from the pigment using osmium tetroxide staining. In this way, the same modelling approach is applied for both 2D masters, simulated and real, and the differences in the subsequent modelling results are then exclusively due to differences in the natures of the masters, i.e. whether it is a simulated structure or a real cross-section. Comparison of the modelling results applied to the SEM cross-section master with the experimental conductivity values also provides the possibility to discuss the individual thermal properties used for modelling. The influence of connectivity in the simulation is seen as a major corrective parameter.

Having examined and corrected the possible shortcomings of the simulated master and confirmed the role of the individual material properties in the model, the remaining difference of the modelled values versus experimental values are exclusively due to the model alone. Here again we identify the importance of connectivity not only as already stated in the simulation but also in the model. By fitting model parameters to account for pigment connectivity to the experimental results, information about the colloidal effects in real coatings, which are neither accounted for in the simulation nor the modelling, can be extracted.

### **Materials**

Pigment-binder systems were studied over a range of binder addition level. The pigment used in the experimental determination of thermal diffusivity was an industry standard slurry-dispersed relatively coarse broad particle size distribution ground calcium carbonate<sup>1</sup> (bcGCC), and the latex was a styrene

<sup>1</sup> Hydrocarb 60 (bcGCC) is a registered trademark of Omya AG

**Table 1.** Summary of the particle data of the materials involved.

	<i>Experimental, Simulation</i>	<i>SEM imaging, Simulation</i>
<b>Latex</b>	<b>SA</b>	<b>SB</b>
Dosages [w/w%]	0*, 4, 6, 8*, 12*, 20*, 25*	2, 6, 10, 14
Diameter [ $\mu\text{m}$ ]	0.20 *Ref. [5]	0.14 Ref. [9]
<b>Pigment</b>	<b>bcGCC</b>	<b>nfGCC</b>
PSD [w/w%]		
< 5 $\mu\text{m}$	93	100
< 2 $\mu\text{m}$	60	95
< 1 $\mu\text{m}$	40	75
$d_{50}$ (weight median) [ $\mu\text{m}$ ]	1.6	0.6

acrylic<sup>2</sup> (SA) having a particle size of 0.2  $\mu\text{m}$  and glass transition temperature,  $T_g$ , of 5°C. In addition, SEM cross-sectional image data from a previous study adopting a similar range of latex addition [9] were used in comparison. The pigment in this latter study was a finer ground calcium carbonate<sup>3</sup> having a narrow particle size distribution (nfGCC), and the latex was styrene butadiene<sup>4</sup> (SB) of particle size 0.14  $\mu\text{m}$  and  $T_g$  20°C. By studying the comparison between particle packing simulation and the SEM images of nfGCC, it is possible to derive the level of confidence, or shortfall, for the simulation. Using the simulation then for the bcGCC correlations with experimental diffusivity determined for the bcGCC could be established. The thermal properties of the constituent components, i.e. pigment and latex, are identical for the calcium carbonate component and only differ slightly for the two lattices used in the coating structure series. A summary of the materials involved is given in Table 1 and the literature values of their respective thermal properties are shown in Table 2.

For the simulations of particle deposition, the particle size distributions of both pigments were expressed as the log-normal distribution, having the cumulative probability distribution function,  $P_w(d)$ , of particle diameter,  $d$ :

<sup>2</sup> Acronal S 360D (SA) is a registered trademark of BASF AG

<sup>3</sup> Covercarb 75 (nfGCC) is a registered trademark of Omya AG

<sup>4</sup> DL966 (SB) is a registered trademark of Dow AG

$$P_w(d) = \frac{1}{2} + \frac{1}{2} \operatorname{erf} \left[ \frac{\ln(d) - \nu}{\sqrt{2\tau}} \right] \quad (1)$$

where the parameters  $\nu$  and  $\tau$  were determined from the weight based particle size distributions of the pigment data sheets. The fitted parameters were  $\nu_{bc} = 0.47000$  and  $\tau_{bc} = 0.89231$  for the bcGCC pigment and  $\nu_{nf} = -0.5108$  and  $\tau_{nf} = 0.9237$  for the nfGCC pigment. Because of the isometric nature of calcium carbonate, the pigment particles could be assumed to be spherical for the conversion of mass (volume) to number occupancy. The number based distribution function becomes then:

$$P_N(d) = \frac{1}{2} + \frac{1}{2} \operatorname{erf} \left[ \frac{3\tau^2 + \ln(d) - \nu}{\sqrt{2\tau}} \right] \quad (2)$$

Figure 1 shows the cumulative probability distribution functions of the actual pigment systems as used in the simulations, containing 818 and 791 particles for the bcGCC and nfGCC, respectively. Because of the very large number of fine particles in the nfGCC systems, the smallest particle diameter for the simulation of those systems was limited to  $d_{\min} = 0.1 \mu\text{m}$  in order to keep the calculation demand in an acceptable range (see “Simulation of Particle Deposition” below). The pigment was initially simulated as hard spheres following the derived size probability distribution function.

The SA binder used in the experimental part, had been shown to act disruptively on the pigment packing both in the bcGCC pigment [5, 8] and the nfGCC pigment [9] at certain low to medium dose ranges, and acting as a hard sphere during consolidation. For the simulations, the binder was

**Table 2.** Summary of the thermal properties of the materials involved.

	Heat Capacity $c_p$ [ $\text{Jkg}^{-1} \text{K}^{-1}$ ]	Thermal Conductivity $k$ [ $\text{Wm}^{-1} \text{K}^{-1}$ ]
<b>Latex</b> – Ref. [10]		
Styrene Acrylate (SA)	559.8	0.21
Styrene Butadiene (SB)	(454.8)*	0.25
<b>Pigment</b> – Ref. [11, 12]		
Calcium Carbonate	880	2.7

\* Literature value for polystyrene. This value is not required for the calculations in this study but given for reference.

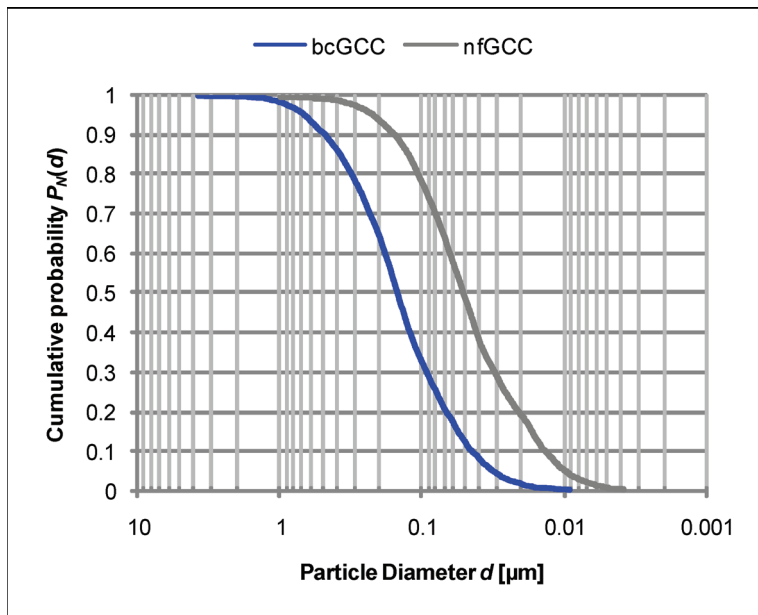


**Figure 1.** Cumulative probability plot for the number based particle size distributions of the bcGCC and nfGCC pigments. The plotted particle systems contain 818 and 791 pigment particles, respectively.

therefore first described as mono-size rigid spheres. Both the measurements of thermal diffusivity and the simulation of the particle deposition were made for the binder-free pigment system as well as for binder concentrations of 4, 6, 8, 12, 20 and 25 w/w% based on pigment. The additional SEM data were from a particle system containing SB binder and was simulated accordingly for binder concentrations of 2, 6, 10 and 14 w/w% based on pigment.

## **Experimental**

### *Tablet forming and measurement of thermal diffusivity*

For the measurement of thermal diffusivity, pigment-binder tablets of the coating colour formulations were formed following the method of Ridgway *et al.* [13]. The coating slurry of initially 65% dry solids content was dewatered by an applied overpressure of 20 bar through a fine membrane (mesh size: 0.025  $\mu\text{m}$ ). The semi-solidified tablets were then fully dried in an

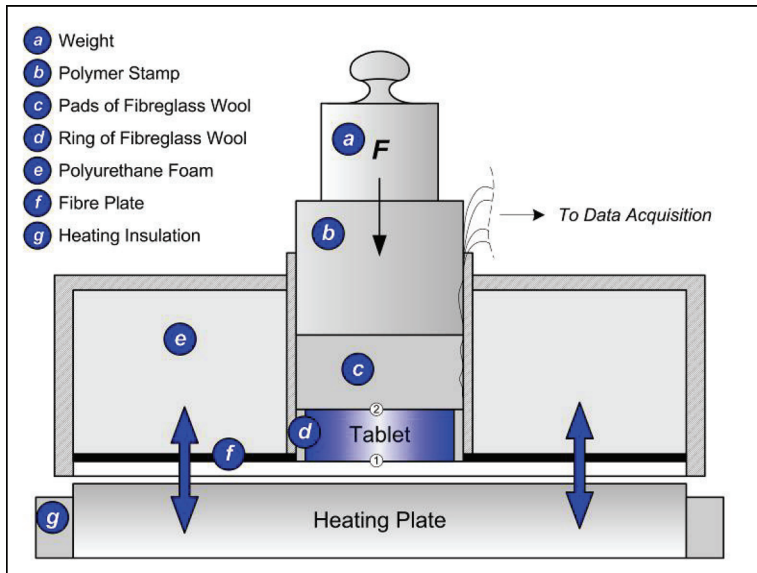


**Figure 2.** Measurement of thermal diffusivity of macroscopic pigment tablets [15].

oven at 60 °C for at least 12 hours. The measurement of thermal diffusivity of the tablet material is based on a technique introduced by Gane *et al.* [14] and further developed by Gerstner *et al.* [15]. The pigment tablets were subjected to a temperature step (contact with a heating plate) on one side while the temperature response on the other side is recorded (Figure 2).

The measured temperature response, along with initial and boundary conditions, allows calculation of the tablet’s thermal diffusivity:

$$D \frac{\partial^2 \vartheta}{\partial z^2} - \frac{\partial \vartheta}{\partial t} = h \cdot (\vartheta - \vartheta_a) \quad (3)$$

where  $D$  is thermal diffusivity [ $\text{m}^2\text{s}^{-1}$ ],  $\vartheta$  is temperature [°C],  $\vartheta_a$  is ambient temperature [°C],  $z$  is the tablet thickness coordinate [m],  $t$  is time [s] and  $h$  is a heat loss term [ $\text{s}^{-1}$ ].

Using the measured tablet densities as well as literature values for the heat capacities of calcium carbonate and n-butyl acrylate for binder (see Table 2), the thermal conductivities of the materials were calculated according to Gerstner *et al.* [5].

### Porosimetry

A portion of each tablet was characterised by mercury porosimetry for both porosity and pore size distribution using a Micromeritics Autopore IV mercury porosimeter. The maximum applied pressure of mercury was 414 MPa, equivalent to a Laplace throat diameter of 0.004  $\mu\text{m}$ . The mercury intrusion measurements were corrected for the compression of mercury, expansion of the penetrometer and, where appropriate, the compression of the solid phase of the sample using the equation of Gane *et al.* [16]. Figure 3 shows the measured pore size distributions.

In Figure 3 we see that the addition of binder at first increases the specific pore volume,  $V$  being expressed as volume per unit weight of sample, and moves the typical pore size from  $\sim 0.1 \mu\text{m}$  to  $\sim 0.2 \mu\text{m}$ . Further binder addition reinforces the increased pore size and progressively reduces specific pore volume until the pores eventually become reduced again in size as the latex effectively fills in the remaining pores as the critical pigment volume concentration is approached.

### Simulation of particle deposition

The simulated particle deposition is a simplified, two dimensional version following the Monte Carlo approach by Vidal *et al.* [17]. At first, a virtual domain is created. The height of the domain is the thickness of the wet

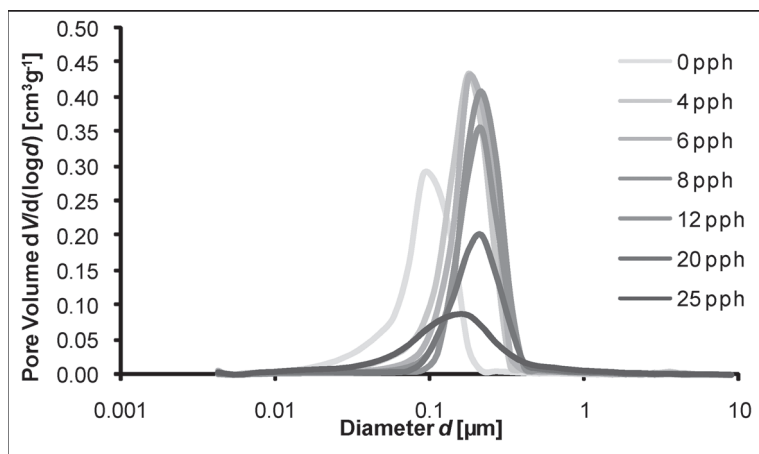


**Figure 3.** Pore size distributions of the bcGCC tablet material at different binder dosages.

coating layer and is based on a specified target coat weight and the specified initial solids content for pigment and latex. For the domain sides, periodic boundary conditions apply. The width of the domain is defined in advance, and comprises a balance of two considerations: on the one hand, the domain must be large enough to provide a sufficient number of particles (to follow the pigment particle size distribution) and also to be larger than the biggest particle present, on the other hand, a small domain reduces the total number of particles and therefore can greatly reduce the calculation demand. It was found that a domain size of  $d_D = 10 \mu\text{m}$  is an acceptable compromise of both aspects. A particle deposition containing ca. 2 000 particles was calculated in less than four hours on a standard office PC.

Table 3 summarizes some basic domain data.

The numerically generated pigment and binder particles are placed evenly at random in the domain as in an idealised dispersed coating colour (Figure 4.a), i.e. ignoring any species interactive effects. The actual particle deposition algorithm applies a minimisation of the particle potential energy in respect to height. Each particle is moved by a small distance in a random, downward oriented direction. In the first series of simulations, the move is accepted if no overlapping with other particles occurs, thus describing the rigid sphere approximation. This iteration is followed for each particle until no particle can be moved for two consecutive iterations; the system is then regarded as deposited (Figure 4.b). The resulting two dimensional quasi “cross-sectional” structures are used as the basis (master template) for the parameter generation of the general Lumped Parameter Model to be used subsequently to calculate the thermal diffusivity.

In order to study the effective thermal connectivity of the structure, identified as being necessary when compared with the experimental data, a slightly different approach was followed in a second series of simulations by allowing slight overlapping of the particles (soft sphere model). This takes account of the irregular shaped pigments, the adsorbed polymer layer (dispersant) and

**Table 3.** Standard data for the domains used in the simulations.

	<i>Domain</i>
Width	10 $\mu\text{m}$
Initial solids content	65 w/w%
Target coat weight	20 $\text{gm}^{-2}$
Binder concentrations	0–25 w/w%
Number of particles	~ 1–3k

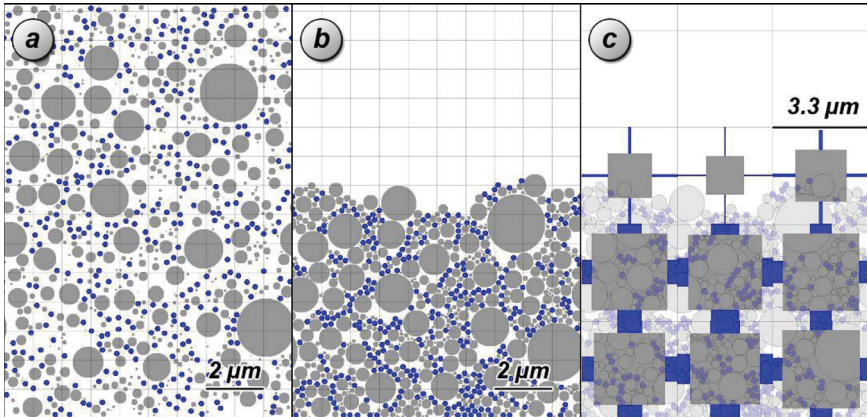


**Figure 4.** a) Initial domain ( $d_D = 10 \mu\text{m}$ ) with randomly distributed particles (8 w/w% binder). b) The same domain after particle deposition and c) the domain split into three lateral sub-domains ( $d_{SD} = 3.3 \mu\text{m}$ ) with a superposed lumped parameter unit cell developed for each sub-domain.

of the action of the consolidation of latex spheres. This approach will be considered in more detail when considering the role of connectivity in initiating transferring thermal contact.

Since both the generation of the pigment particles and the particle deposition process are of a statistical nature, four replicates were calculated for each configuration.

### **Modelling of effective thermal conductivity (simulation master)**

After deposition of the particles in the domain, it is split into several sub-domains. For each sub-domain a unit-cell of the Modified Lumped Parameter Model (Figure 5) is superimposed. The unit-cell permits the calculation of the effective thermal conductivity of the coating structure [18]. The following section introduces the Lumped Parameter Model in more detail including the effect of sub-domain size on the effective properties subsequently derived.

#### *The Lumped Parameter Model (LPM)*

Each unit cell is based on the Lumped Parameter Model proposed by Hsu *et al.* [19]. The effective thermal conductivity of each unit cell is calculated by

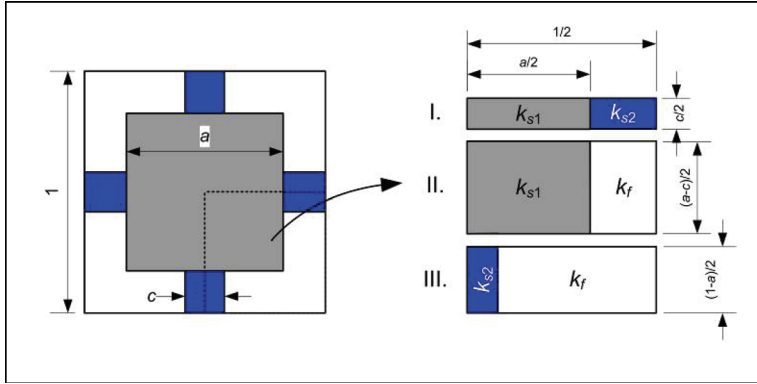


**Figure 5.** Unit cell of the modified lumped parameter model [18].

splitting up the cell structure into an arrangement of serial and parallel thermal resistors.

The unit cell consists of a first, square, solid phase  $k_{s1}$  that represents the pigment. Its size is controlled by the pigment variable  $a$ . Placed as a proportion of material contact with the pigment is a second solid phase  $k_{s2}$ , representing the binder. The width of the “binder bridges” is defined by the binder variable  $c$ . The rest of the unit cell is filled with air (fluid,  $f$ )  $k_f$ . The total effective thermal conductivity  $k_e$  of the unit cell for  $c < a$  is then given by:

$$\frac{k_e}{k_f} = \frac{c}{(\lambda - \mu)a + \mu} + \frac{a - c}{(\lambda - 1)a + 1} + \frac{1 - a}{(\mu - 1)c + 1} \quad (4)$$

where  $\lambda (= k_f/k_{s1})$  is the conductivity ratio of the fluid phase to the pigment phase, and  $\mu (= k_f/k_{s2})$  is the conductivity ratio of the fluid phase to the binder phase. For the conductivities of the individual phases, the appropriate literature values are used [10, 11, 12]. The original domain of the deposited particle system (Figure 4.b) is divided into several square sub-domains for each of which the variables  $a$  and  $c$  are calculated individually. The pigment variable  $a$  is given by the relative pigment area  $A_p$  in a sub-domain:

$$a = \sqrt{A_p} \quad (5)$$

and the binder variable  $c$  can be calculated by the definition of the unit cell porosity (see Figure 5):

$$\phi(a,c) = 1 + 2ac - 2c - a^2 \quad (6a)$$

$$c(a,\phi) = \frac{\phi - 1 + a^2}{2(a-1)} \quad (6b)$$

In this way, the porosities of the model unit cells equal the porosities of the structural sub-domains. The resulting unit cells can then be assigned to the according sub-domain in the coating structure (Figure 4.c) to calculate the overall porosity and effective thermal conductivity. The same approach will be followed to generate the model parameters  $a$  and  $c$  based on image analysis of cross-sectional SEM images of coatings.

In order to exclude effects of surface roughness and surface porosity of the simulated structures, when calculating the overall properties of the coating structure, the top or boundary layer in the coating structure (compare Figure 6.a) is determined as the uppermost row of unit cells with a porosity of not larger than 35%. In Figure 4.c, for example, only the two lower rows of unit cells would be used for calculation of the overall properties.

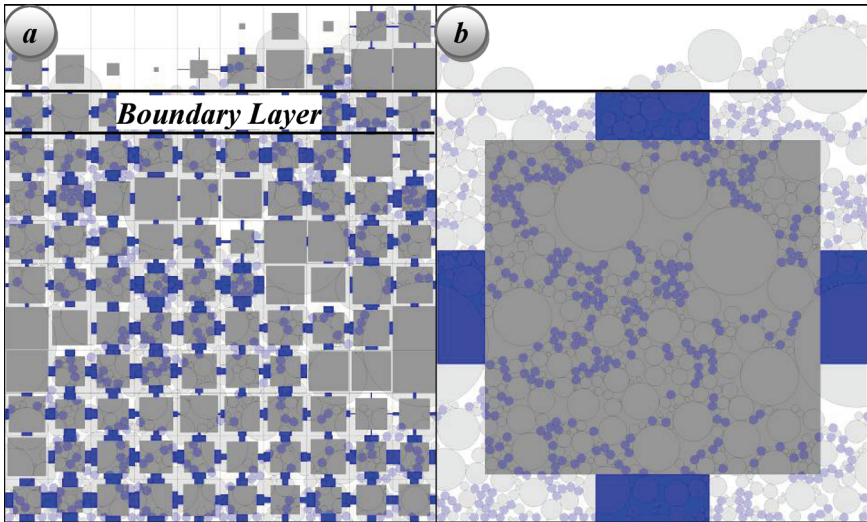


**Figure 6.** a) Domain split into ten lateral sub-domains and unit cells for each sub-domain. b) The same domain with a single sub-domain and unit cell.

*The effect of sub-domain size*

The number of lateral sub-domains in both a simulated structure and SEM cross-sections, and therefore the number of unit cells, does have an influence on the calculation of specific values of thermal conductivity. A large number of sub-domains (smaller sub-domains, Figure 6.a), generates more information on the homogeneity and isotropy of the coating structure but it is more susceptible to those irregularities, whereas larger sub-domains can even out inhomogeneities (Figure 6.a).

Figure 7 shows the calculated effective thermal conductivity of the simulated coating structure, i.e. the entire domain ( $d_D = 10 \mu\text{m}$ ), as a function of the sub-domain size  $d_{SD}$ . For large sub-domains (one, two, three or four lateral sub-domains), the calculated thermal conductivity is fairly constant. When the sub-domain size is in the area of the pigment particle size ( $d_{SD} = 2 \mu\text{m}$ , 5 lateral sub-domains), there is a distinct drop in the calculated values. Another drop occurs at the general size of the binder particles, confirming that sub-domains smaller than the present particle sizes are more susceptible

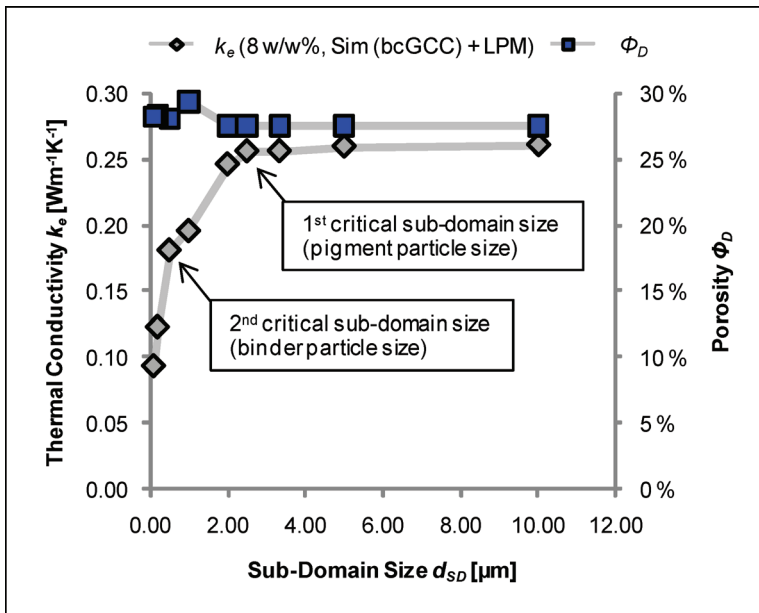


**Figure 7.** Effective thermal conductivity and porosity of a simulated coating structure obtained in combination with the Lumped Parameter Model as a function of the sub-domain size.

to “weak spots” in the structure. This can be observed in Figure 6.a, where the sub-domain size is  $d_{SD} = 1 \mu\text{m}$ . Some sub-domains are entirely filled by pigment, whereas others show a high binder amount or, conversely, a high porosity.

Similar to Figure 7, Figure 8 shows the calculated effective thermal conductivity of the SEM cross-sectional coating structure (see next chapter). The same trend as in Figure 7 can be observed, although the drop in the thermal conductivity does not occur as distinctly as for the simulated structure. This is most likely due to the more random nature of the pigment and binder areas in the cross-sectional cuts, compared to the mathematically defined particle size distribution of the simulated structures. However, both figures show that a sub-domain size of  $d_{SD} = 3.3 \mu\text{m}$  (three and six lateral sub-domains for simulation and SEM images, respectively) is above the critical sub-domain size, while it still provides information on the homogeneity and isotropy of the structures. For future calculations a sub-domain size of  $d_{SD} = 3.3 \mu\text{m}$  will be used.

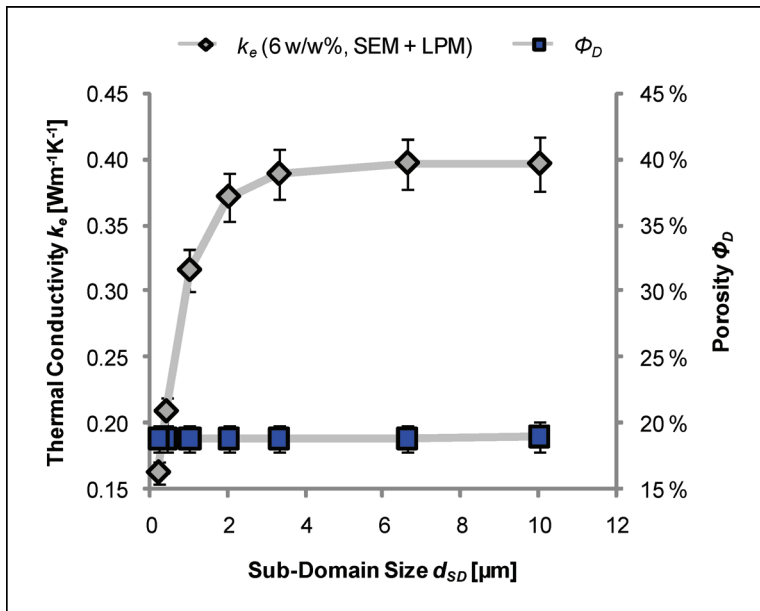


**Figure 8.** Effective thermal conductivity obtained by SEM imaging in combination with the Lumped Parameter Model as well as porosity as a function of the sub-domain size. The porosity is determined as the average void area fraction of the unit cells in an SEM cross-section image.

Furthermore, Figure 7 and Figure 8 show the porosities calculated as the void area fractions of the simulated and of the SEM cross-sectional structures. The simulated porosity remains largely independent of the sub-domain size. As it is the porosity of the simulation domain, it is quite clear that the simulated pore area in the domain does not change by decreasing the sub-domain size. However, by changing the sub-domain size in simulated domains, the position of the boundary layer changes slightly. This is the reason for the kink in the porosity curve of Figure 7.

### **SEM cross-section imaging and thresholding (SEM master)**

The SEM cross-section images were provided from a previous study [9] as a means to compare the simulated particle structures to real cross-sectional data. The methodology and equipment used is described in [20]. A high resolution field emission scanning electron microscope (FE-SEM, Jeol JSM 6335 F) was used in the element contrast mode (backscattered electron detection). The samples were prepared using the same tablet forming techniques as described above. The SB latex was made visible by a treatment with osmium tetroxide. Figure 9 shows a cross-sectional image of a tablet containing 6 w/w% binder. In this image, the pores are distinguished as dark areas whereas the stained latex appears bright. Thresholding was used to identify clearly the three different phases.

Many different thresholding techniques exist, not least because of the great

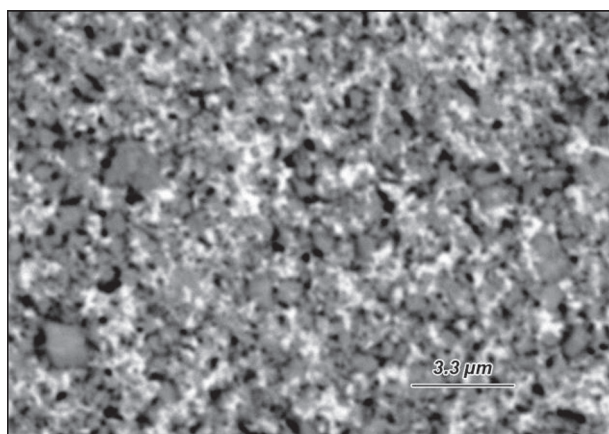


**Figure 9.** Original SEM image of a 6 parts latex tablet structure. The  $\text{OsO}_4$  stained latex appears in a brighter tone.

variety of application fields and their individual requirements. For the thresholding of the SEM images a one-dimensional maximum entropy based algorithm based on the work of Kapur *et al.* [21] was used. Because of the three phases present, two thresholds need to be found: the air-pigment threshold  $t_1$  and the pigment-binder threshold  $t_2$ . Let  $P_i$  be the normalised histogram of the grey level image, where  $0 \leq i \leq L - 1$  for  $L = 256$  grey levels, then the total entropy  $f_2$  of the histogram, segmented by  $t_1$  and  $t_2$ , is given by:

$$f_2(t_1, t_2) = H(0, t_1) + H(t_1, t_2) + H(t_2, L) \quad (7)$$

where the entropy  $H(a, b)$  of a histogram segment from  $a$  to  $b$  is:

$$H(a, b) = - \sum_{i=a}^b \frac{P_i}{\omega(a, b)} \ln \frac{P_i}{\omega(a, b)} \quad (8)$$

and:

$$\omega(a, b) = \sum_{i=a}^b P_i \quad (9)$$

The optimal thresholds are the grey levels that maximize the total entropy of equation 7. The normalized histogram  $P_i$  is based on the grey level data of a single SEM image. For each binder level, 25 cross-sectional images were analysed. Figure 10 shows the threshold image for an air-pigment threshold of  $t_1 = 77$  and a pigment-binder threshold of  $t_2 = 163$ .

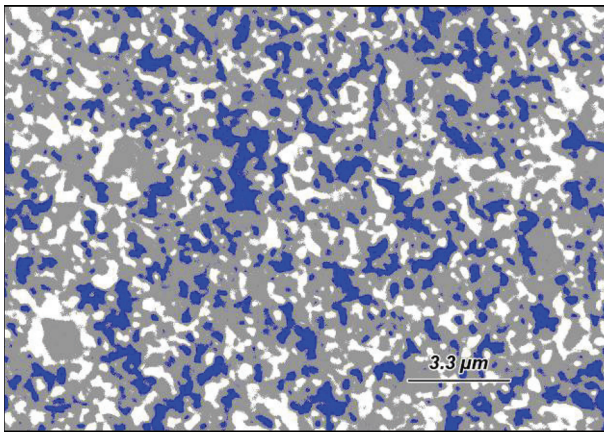


**Figure 10.** Threshold image. For a better comparison, the phases are colour coded as in the simulated structures (compare Figure 4.b).

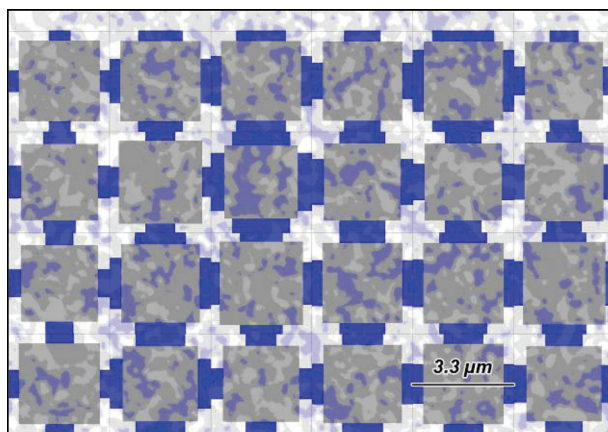


**Figure 11.** Unit cell image. Superposition of LPM unit-cells onto the SEM threshold image.

After identifying the phases of pigment, binder and air in the SEM images, the unit-cells of the Lumped Parameter Model were superimposed onto the cross-sectional image according to the local area of the respective phases. Figure 11 shows the unit cell image of the same cross-section as in Figure 10. It can be seen that the unit cell parameters for pigment and binder follow the local concentrations of the phases as identified by the thresholding.

## RESULTS AND DISCUSSION

### The effect of binder content

#### *Experimental and simulated structures*

Figure 12.a shows the thermal conductivities calculated from the thermal diffusivity measurement of the tablet material (experimental) as well as the numeric effective thermal conductivity calculated for the lumped parameter unit cells of six ( $2 \times 3$ ) sub-domains in the equivalent hard sphere simulated coating structure. There is a clear difference in the general level of thermal conductivity. This difference can be only partially accounted for by the porosity differences between the simulated two-dimensional structures and the experimental porosity (Figure 12.b). This finding reconfirms the non-trivial relationship between the two dimensional void area and the three dimensional pore structure [9, 20], but, despite the better agreement on porosity at binder levels below 10 w/w% the difference in conductivity in this region is at

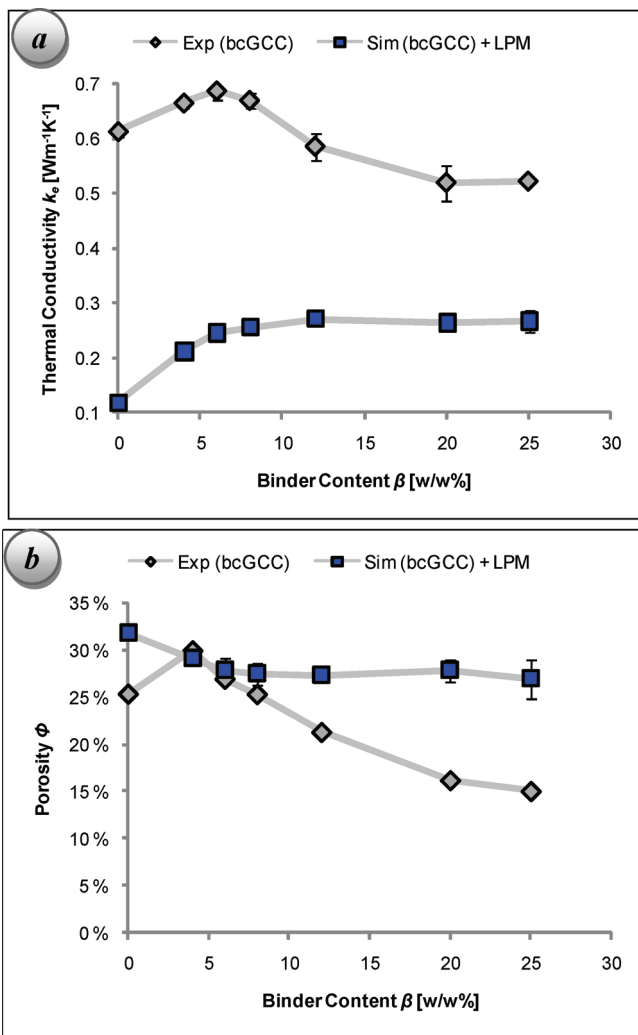


**Figure 12.** a) Effective thermal conductivity of the bcGCC coating structures measured experimentally from tablet material and calculated numerically by application of the lumped parameter model to simulated deposited hard sphere particle system. b) Porosity of bcGCC coating structures measured experimentally by mercury porosimetry, and porosity calculated as the simulated void area fraction over all sub-domains as a function of binder content.

its greatest. This initial gap between experimental and numeric will be given special attention as it relates to the connectivity differences (see Connectivity of Coating Structures) between perfect spheres and the real situation of pigment particle asymmetries and the important role of adsorbed dispersant polymer (polyacrylate) used during the pigment slurry manufacture.

A peak in the experimental thermal conductivity (Figure 12.a) occurs for a binder content of 6 w/w%. Below this packing-critical binder concentration, the connectivity of the structure increases by adding binder, and the positioning of latex at the pigment contact points in the real experimental case leads to a disruptive packing effect. Above the critical disruption concentration, the rigid latex particles start to fill the structural voids, and, due to its inherent insulating property, progressively lower the effective thermal conductivity. This is consistent with earlier work by Ridgway and Gane [7], showing the disruptive interaction of latex in the viscosity response of coating colours, and also with work by Gane *et al.* [9] showing the pigment disruption in OsO<sub>4</sub>-stained cross-sectional SEM images. In contrast to the experimental conductivities, the numeric values show a monotonic increase in thermal conductivity up to a binder concentration of 12 w/w%. This difference is most likely initially due to the missing connectivity in the simulation between the pigment particles, but which occurs in real systems due to particle anisotropy and adsorbed dispersant polymer. In the simulation, therefore, conductivity keeps increasing upon adding binder until the maximum connectivity (of the unit cell) is reached at very high binder levels, and from thereon conductivity reduces by adding more binder. The generally large difference to the experimental results requires further discussion and a discussion of necessary reality-driven corrective factors.

### *SEM cross-section images*

Figure 13 shows the results obtained by superposition of the Lumped Parameter Model unit-cells onto the thresholded SEM cross-sectional images. It should be kept in mind, however, that in Figure 13, different types of particle systems are compared: the experimental values are from the bcGCC system with SA latex and the SEM images relate to the nfGCC system with SB latex. Since the material properties of both the experimental and the modelled SEM system should be identical for the pigment and very similar for the binders concerned (compare Table 2), three possible reasons for the difference of the curves in Figure 13.a come to mind:

- a) The two experimental coating structures are fundamentally different, especially in the lower range of binder dosages.

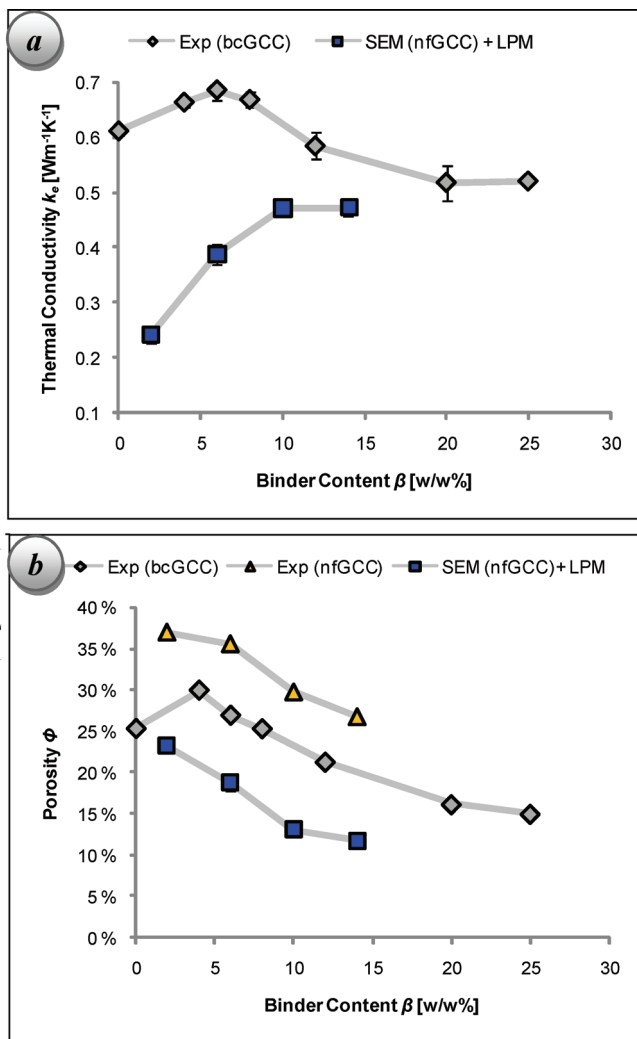


**Figure 13.** a) Effective thermal conductivity of the coating structure measured experimentally from tablet material (bcGCC, SA latex) and calculated numerically by application of the lumped parameter model compared to that applied to SEM cross-sectional images (nfGCC, SB latex). b) Porosity measured experimentally by mercury porosimetry (both bcGCC and nfGCC) and porosity calculated as the void area fraction over all sub-domains as a function of binder content from the SEM images (nfGCC, SB latex).

- b) There is a general discrepancy caused by the interpretation of the coating structure by the LPM.
- c) The literature material values chosen for modelling differ from the actual material properties.

In contrast to Figure 12, no particle simulation is involved, rather it is merely the application of the model to a real coating structure (SEM master). It can be noted in Figure 13.a that the predicted thermal conductivities by the model are initially still lower than the experimentally measured ones. Also the cross-sectional porosities, or void areas, are lower than the ones measured by mercury porosimetry, even though the trend of decreasing as a function of higher latex dose is followed very well.

It is unlikely that the difference of bcGCC and nfGCC (point a)) is accountable for the large difference in thermal conductivity seen in Figure 13. Especially since the difference is even larger in Figure 12 for the same pigment/binder system.

As for point c), one can see for the higher binder contents in Figure 13.a that both curves are approaching a common level of ca.  $0.5 \text{ Wm}^{-1}\text{K}^{-1}$ . This is a good indication that the material value for binder in the model is of the right magnitude. This was not obvious, since Figure 12.a showed a very large difference even for higher binder contents. Neither can the initially large difference in thermal conductivity be accounted for by the material value of pigment, since it is identical. Assuming an infinitely high conductivity of pigment, equation 4 reduces to:

$$\frac{k_e}{k_f} = \frac{c}{\mu(1-a)} + \frac{c-a}{a-1} + \frac{1-a}{(\mu-1)c+1} \quad (10)$$

The point for 6 w/w% binder in the SEM data has an average lumped parameter model pigment factor of  $a = 0.7884$  and binder variable  $c = 0.3600$ . For these unit cell properties, the maximum effective thermal conductivity (for a superconductive pigment) becomes  $k_e^{\text{max}} = 0.4156 \text{ Wm}^{-1}\text{K}^{-1}$ . This is still significantly lower than the experimental value. In fact, this example illustrates the great influence of the connecting phase (binder bridges in this stage of the LPM) in the effective thermal conductivity. As the interpretation of connectivity by the model is crucial, point b) of the possible reasons seems most plausible and a further discussion on connectivity is required in order to improve the simulation and to understand better the role of pigment and binder addition.

### Connectivity of coating structures

The previous discussion regarding the simulated and experimental values showed a significant difference in thermal conductivity between observed and the LPM modelled structure, mainly at low binder concentrations or binder free systems. It was hypothesised that this difference is due to the differences in connectivity of the structures. Figure 14 shows a hard sphere simulated binder free particle system; the domain alone is seen in Figure 14.a, the domain and the superimposed LPM unit cells shown in Figure 14.b. Figure 14 illustrates that the problem of connectivity is twofold.

At first, we note that the particles in the simulations are ideal circles; they only have point contacts to other particles, which is theoretically equivalent to no contact area at all. This is in contrast to real pigment particles having irregular particle shapes and shape distributions as well as adsorbed dispersant polymer on the pigment surface. Both factors effectively create a larger pigment-pigment interface, or pigment connectivity. This difference in connectivity of a binder free system is due to the nature of the simulation using rigid, ideal spheres. It is the zero conductivity difference of the simulation,  $\Delta k_0^S$ .

The second difference in connectivity is directly due to the nature of the Lumped Parameter Model. The original approach restricts connectivity to the binder phase alone. If no or little binder is present, there are no

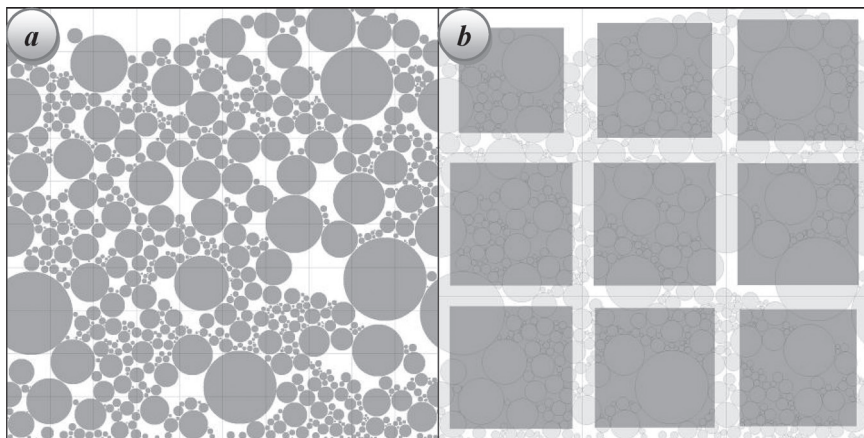


**Figure 14.** a) Domain of a simulated binder free coating structure. b) The same domain with superposition of the LPM unit cells. The lack of connectivity in the model is responsible for the zero value of calculated conductivity.

connecting bridges per se to take the pigment connectivity into account (see Figure 14.b), even if there were area contact between simulated pigment particles. As the previous discussion showed, this difference can be quite significant and it is not related to the cross-section (whether it is simulated or it is an SEM image), but to the model. It is the zero conductivity difference of the model,  $\Delta k_0^M$ . The total initial difference in conductivity,  $\Delta k_0$ , (for the binder free system) in Figure 12.a, is thus

$$\Delta k_0 = |k_e(0) - k_s(0)| \quad (11)$$

and can be expressed as

$$\Delta k_0 = \Delta k_0^S + \Delta k_0^M \quad (12)$$

The following sections will first examine ways to quantify the connectivity differences of simulated coating structure and model for binder free systems before the connectivity of binder will be further discussed.

### *Connectivity of the simulation*

It was pointed out that the difference in structural connectivity is due to the irregular shape of real pigment particles as well as the presence of adsorbed dispersants on the pigment surfaces. With a certain amount of overlapping, the point contacts between the particles will extend to contact areas. This contact area approach can be done without modifying the deposition algorithm. Merely a modification of the overlapping condition is required to make the particles seem smaller due a “soft” surface layer. The thickness of the soft layer  $s_A$  is based on the absolute size, the radius  $r_A$ , of a particle  $A$ :

$$s_A = \xi_A \cdot r_A \quad (13)$$

where  $\xi_A$  is the overlap factor, a coefficient of softness. Larger pigment particles appear therefore “softer” to account not only for the adsorbed poly-dispersant but also for the irregular shape of pigment particles. The overlapping condition for two particles  $A$  and  $B$  becomes then:

$$\sqrt{(x_A - x_B)^2 + (z_A - z_B)^2} \leq r_A(1 - \xi_A) + r_B(1 - \xi_B) \quad (14)$$

where  $\xi_A = \xi_B$  if  $A$  and  $B$  are of the same material.

While soft particles will have a contact area, the porosity will also be reduced because the particles will form a denser packing. Porosity can there-

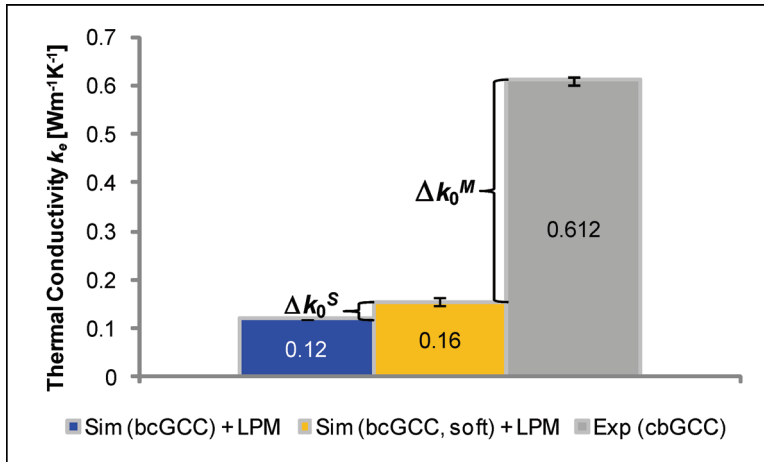


**Figure 15.** Effective thermal conductivities for simulations with rigid pigment spheres and soft pigment spheres ( $\xi_{st} = 3\%$ ) as well as the experimental thermal conductivity for the binder free pigment structure.

fore be used as the control parameter to identify the overlap factor of pigments. Figure 12.b shows an experimentally measured porosity of 25% versus a simulated area porosity of 32% for the simulated structure. The question is what overlap factor (softness of pigments) would be required to match the experimental porosity at zero binder level. By performing a series of particle depositions with varying overlap factors, it was found that for a pigment overlap factor of  $\xi_{st} = 3\%$  the porosity of the binder free simulated packing largely matches the experimental porosity. Figure 15 shows the calculated effective thermal conductivities for the simulation with rigid spheres and with a soft sphere packing to match the experimental porosity as well as the experimentally measured conductivity. It is seen that the zero conductivity difference of the simulation  $\Delta k_0^S$  is much smaller compared to the remaining difference  $\Delta k_0^M$  accounted for by the model connectivity. It is therefore vital to discuss the pigment connectivity and its role in the LPM. This will be done in the following section, Developing Connectivity of the Model.

### *Applying particle overlap to simulation*

In addition to the soft sphere approach for pigments, it can be extended to the binder as well. The binder phase is much softer and is likely to form interdiffused layers where binder particles touch. To reflect this, the binder would

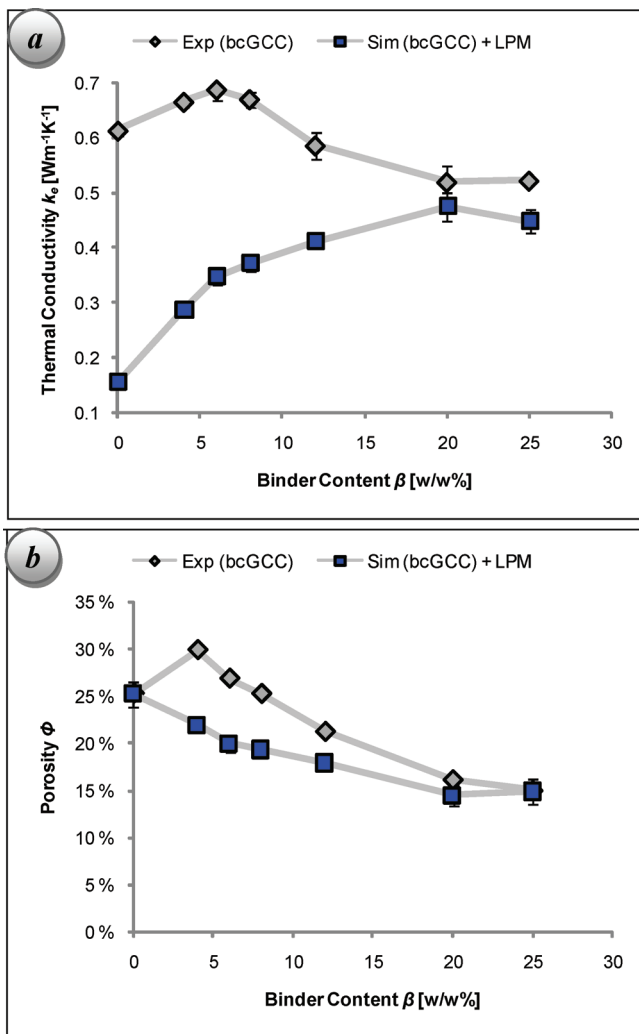
need a higher overlapping factor compared to pigment. Figure 16 shows the same comparison of experimental values and simulated values as in Figure 12, but the particle deposition is now made allowing an overlap of  $\xi_{s1} = 3\%$  for pigment and  $\xi_{s2} = 40\%$  for binder. While the general shape of the simulated thermal conductivity curve does not change compared to Figure 12.a, the thermal conductivities of the higher binder levels approach the experimental values and are similar to the level seen in Figure 13.a. This reconfirms the choice of the material value for binder and points out that the large conductivity difference (of higher binder levels) in Figure 12.a is due to the deficiencies of the hard sphere approximation simulated structure.

Figure 16.b shows that the porosities for the system allowing particle overlap, agree better with experimental values, especially at higher binder levels. Despite the generally better agreement for higher binder contents, the thermal conductivities of lower binder levels are still distinctly less than the experimental values. Because the conductivity difference of the simulated structure is accounted for in this curve, the remaining difference is that caused by the connectivity interpretation of the Lumped Parameter Model alone.

### *Developing connectivity of the model*

In the original approach of the Lumped Parameter Model, it is only binder that provides connectivity. The absence of any means to connect the unit cells of binder free systems (see Figure 14.b) leads to an underestimation of thermal conductivity compared to real systems. The remaining conductivity difference  $\Delta k_0^M$  is therefore the missing pigment connectivity which needs to be included in the model. This can be done by introducing “pigment bridges” to connect the unit cells instead of or in addition to binder bridges. This is an inverse mathematical problem of the system of equations (4) and (6.b) which need to be transposed to  $a' = f_a(k_e, c')$  where  $c' = f_c(\phi, a')$  so that for a given effective thermal conductivity  $k_e$  (the experimental value) and a given unit cell porosity  $\phi$  the new pigment factor  $a'$  and the pigment connectivity variable  $c'$  are returned. In other words, it is the question of what amount of pigment needs to be shifted from the central pigment phase to the bridging function in order to get the measured thermal conductivity while maintaining the unit cell porosity. This is illustrated qualitatively in Figure 17.a. Note that if the central phase and the bridging phase are of the same material, it gives  $\mu = \lambda$  and equation (4) simplifies. Still, the calculations involve solving a fourth degree polynomial equation. Hence, there will be four different solutions of which at least one should be physical.

When using the soft sphere approach for the bcGCC system and allowing a pigment overlap of  $\xi_{s1} = 3\%$ , the sub-domains of the binder free structures



**Figure 16.** a) Effective thermal conductivity of the coating structure measured experimentally from tablet material and calculated numerically by application of the lumped parameter model to simulation deposited particle system with the soft sphere approach ( $\zeta_{s1} = 3\%$ ,  $\zeta_{s2} = 40\%$ ). b) Porosity measured experimentally by mercury porosimetry and porosity calculated as the void area fraction over all sub-domains for the soft sphere approach as a function of binder content.

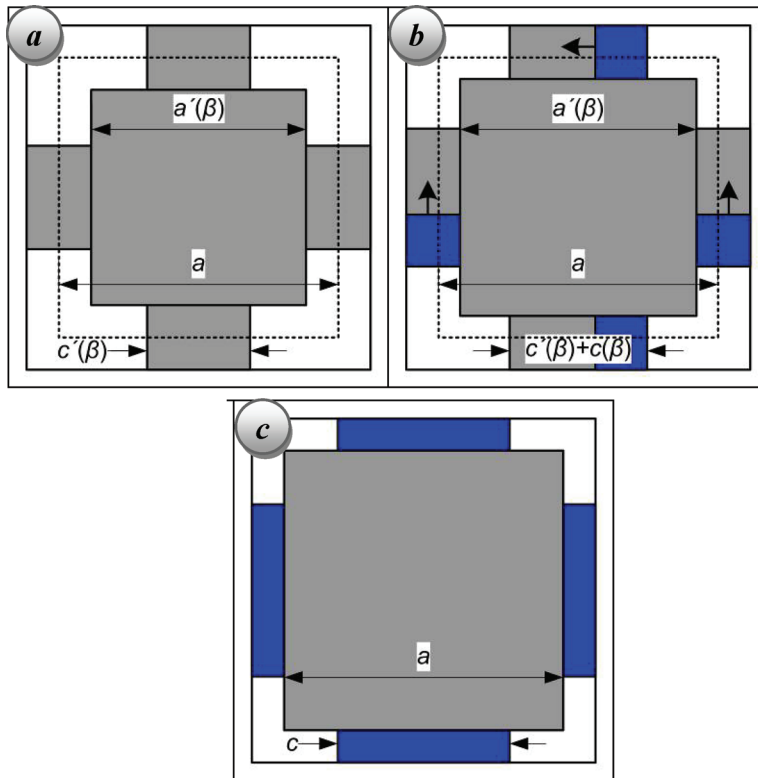


**Figure 17.** a) Corrected pigment factor  $a'$  and new pigment connectivity variable  $c'$ . b) Replacement of pigment connectivity  $c'$  by binder connectivity  $c$ . c) Binder connectivity

have an average porosity of ca. 25% and an average pigment factor of  $a = 0.8643$  for the original unit cells. To reach the experimentally measured thermal conductivity of  $k_e = 0.6 \text{ Wm}^{-1}\text{K}^{-1}$  at constant porosity, the corrected pigment factor becomes  $a' = 0.8225$  along with the new pigment connectivity variable of  $c' = 0.1926$ . This is merely the initial pigment connectivity of the binder free system since both  $a'$  and  $c'$  are a function of the binder dosage. When increasing the binder dosage, the total connectivity increases. In terms of the unit cell it means that the width of the connecting bridges increases. However, while doing so, part of the pigment connectivity is being replaced by binder connectivity, effectively shifting some of the connecting pigment back to the central pigment phase (Figure 17.b). This could be an explanation

for the maximum of thermal conductivity observed for the experimental values. Starting with pigment connectivity only, the binder-induced connectivity, and therefore the total conductivity, is increasing when adding binder. Since at the same time, the pigment connectivity is continuously replaced by binder, the thermal conductivity goes through a maximum when the inherently lower conductivity of binder begins to dominate the total connectivity of the structure. Further addition of binder does increase the connectivity (width of the bridges in the unit cells), but it lowers the conductivity because of the insulating nature of binder compared to pigment. However, as we shall see later, this proposal does not account totally for the local magnitude of the maximum.

### **Comparison of simulated structures with SEM cross-sections**

So far the discussion has focused on the calculated values of the Lumped Parameter Model for the simulated structures and the SEM cross-sections in relation to the experimental values. But in order to characterise the particle deposition simulation independently of the model, it is required to compare the model data for the SEM cross-sectional images directly with the model data of the corresponding simulated structures. This comparison is given in Figure 18. The simulations were done using the same overlapping parameters as for the bcGCC system ( $\xi_{s1} = 3\%$  for pigment and  $\xi_{s2} = 40\%$  for binder) and, for the model calculation, the original LPM approach allowing merely binder connectivity was used. With the exception of the 10 w/w% binder point, the thermal conductivities for calculated SEM cross-sections and simulated structures, as shown in Figure 18.a, agree remarkably well. The previous discussion showed the great influence of the binder connection phase on effective thermal conductivity. The fact the thermal conductivities agree so well for both approaches is, therefore, an indication that the binder amount in the SEM cross-section images was correctly identified by the thresholding algorithm. The calculated porosities, shown in Figure 18.b, differ slightly more for 10 and 14 w/w%. This difference, as also their difference compared to the experimental values, shows once again the problem of comparing two dimensional void areas to three dimensional pore volumes [9].

### **Colloidal effects**

When adding the functionality of pigment connectivity to the unit cell of the LPM, as it was described earlier and was shown in Figure 17.b, the equation (4) extends to:

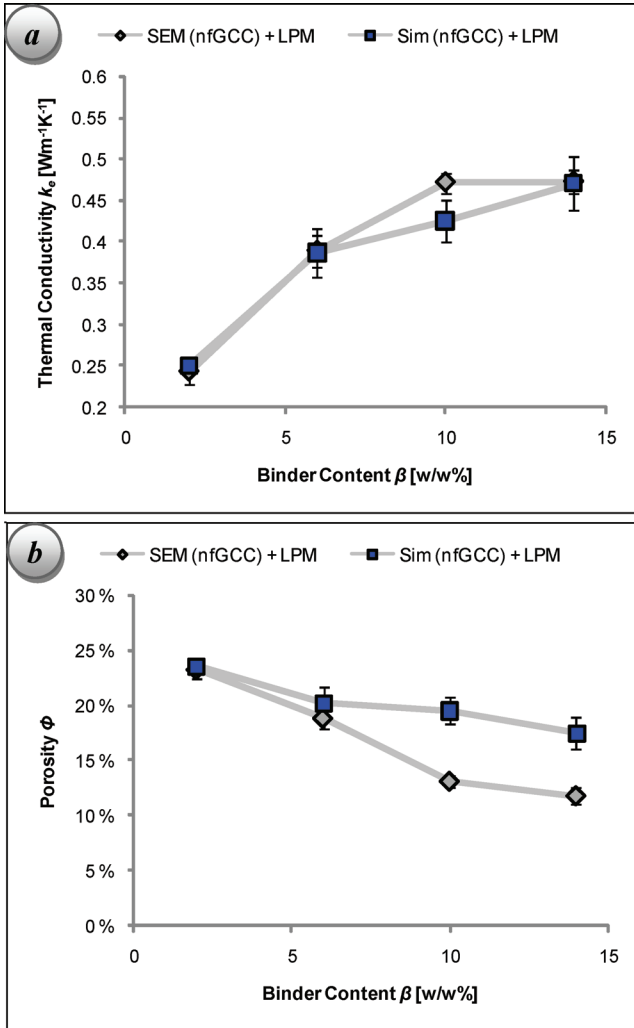


**Figure 18.** a) Effective thermal conductivities calculated with the Lumped Parameter Model for both the SEM cross-sectional images and for the corresponding simulated domain with the soft sphere approach ( $\zeta_{s2} = 3\%$ ,  $\zeta_{s2} = 40\%$ ). b) Porosity calculated as the void area fraction over all sub-domains for the SEM cross-sectional images and the simulated domain using the soft sphere approach.

$$\frac{k_e}{k_f} = \frac{c'}{\lambda} + \frac{c}{(\lambda - \mu)a' + \mu} + \frac{a' - c' - c}{(\lambda - 1)a' + 1} + \frac{1 - a'}{(\lambda - 1)c' + (\mu - 1)c + 1} \quad (15)$$

Furthermore, the definition of unit cell porosity changes to:

$$\phi(a', c') = 1 + 2a'(c' + c) - 2(c' + c) - a'^2 \quad (16)$$

Both equations form a fifth order polynomial system which can be solved numerically to fit the effective modelled thermal conductivity of a unit cell to the experimentally measured thermal conductivity. The unit cell is defined by the void area fraction (porosity) as well as the area fractions of pigment and binder. With the given area fraction of binder that forms the binder

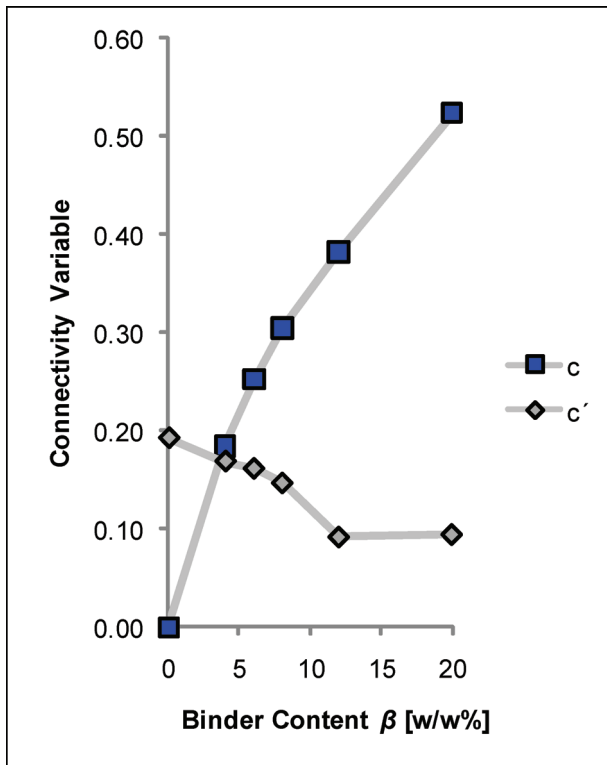


**Figure 19.** Extended unit cell pigment connectivity  $c'$  and binder connectivity  $c$  as a function of binder content.

connectivity, one can calculate the pigment connectivity  $c'$  required to achieve the experimentally measured thermal conductivity for the corresponding pigment and void area fractions of the unit cell. Figure 19 shows the calculated pigment connectivity  $c'$  along with the given binder connectivity  $c$  of the unit cells for different binder dosage. It can be seen that, in contrast to the earlier prediction, the pigment connectivity  $c'$  decreases for binder concentrations up to 8 w/w% and then levels at higher binder contents. The fact that the pigment connectivity at the initial addition of binder is lowered reconfirms the observations made by Gane *et al.* [9]. For low concentrations of binder, colloidal forces drive the latex particles away from the bulk water phase of the forming pores towards the pigment contact points. This effective rejection of the binder from the liquid phase of the pigment results in a disruption of the pigment packing for lower concentrations of latex particles and this is the reason for a decrease in pigment connectivity factor  $c'$  for those concentrations. This captures, in essence, the effect of observed depletion flocculation. For higher concentrations of binder, the phase separating placement of latex particles at pigment contact points reduces, as the colloidal force imbalance of latex particles in presence of other latex particles will be smaller as the environment contains more binder. Pigment connectivity will therefore stabilise itself at higher binder contents.

## CONCLUSIONS

A Monte Carlo simulation-based particle deposition was used to create two-dimensional coating structures which acted as the master for the parameters of a Lumped Parameter Model for the calculation of thermal conductivity. Additional comparison was made between the simulated structure and cross-sectional SEM analysis of coating structures, providing information concerning the limitations in correlation between the simulation assuming a hard sphere model and the experimental projected area porosity. Identifying that hard sphere simulation underestimates the contact area of pigment, due to the adsorbed polymer dispersant layer and particle surface irregularity, it was possible to define a pigment particle overlap for the case when no binder is present. Compressibility of the binder further contributes to the connectivity arising from the presence of the binder. This has particular relevance to the Lumped Parameter Model, for which a modified set of parameters was defined incorporating both connectivity factors based on both pigment and binder overlap.

Surface and colloid chemistry factors cause binder to accumulate first at pigment nodal points, which causes a disruption of the pigment packing up

to 8 w/w% binder. It was shown by fitting the modelled thermal conductivities to the experimental values that the pigment connectivity is in fact lowered at the binder concentrations for which pigment disruption occurs. It is proposed, therefore, that these methods of imaging, pore structure analysis and thermal conductivity can be used to identify and parameterise subtleties in connectivity in real colloiddally interactive particulate systems, based on deviations between simulations and modelling, and experimental values.

## ACKNOWLEDGMENTS

The authors would like to thank Mikko Salo and KCL Keskuslaboratorio Oy for providing the SEM images. Thank you to Kaarlo Nieminen for his assistance in developing the thresholding algorithm and the solution of the equation system for the inverse Lumped Parameter Model. The financial support of TEKES, the Finnish Funding Agency for Technology and Innovation, is gratefully acknowledged. This work was done as part of the project “Thermal Effects and Online Sensing” (THEOS).

## REFERENCES

1. J. Paltakari. Internal and External Factors Affecting the Paper Drying Process, Doctoral Thesis, Helsinki University of Technology, Espoo, 2000.
2. R. H. Hestmo and M. Lamvik. Heat Transfer During Calendering of Paper. *J. Pulp Paper Sci.* **28**(4):128–135, 2002 .
3. P. Gerstner and P.A.C. Gane. Considerations for Thermally Engineered Coated Printing Papers: focus on electrophotography. In proc. *Iarigai 35<sup>th</sup> International Research Conference of Advances in Printing and Media Technology*, Valencia, Spain, 2008.
4. S. Rousu, T. Grankvist and D. Eklund. The Effect of Polymers on the Final Coating Structure. In proc. *Tappi 2001 Advanced Coating Fundamental Symposium*, pp. 199–209, San-Diego, CA, USA, Tappi Press, Atlanta, 2001.
5. P. Gerstner, J. Paltakari and P.A.C. Gane. Measurement and Modelling of Heat Transfer in Paper Coating Structures. *J. Mater. Sci.*, **44**(2):483–491, 2009.
6. Encyclopædia Britannica Online, Academic Edition, Merriam-Webster Dictionary & Thesaurus, <http://search.eb.com/>, Cited 24.09.2008.
7. C.J. Ridgway and P.A.C. Gane. Effect of Latex and Pigment Volume Concentrations on Suspension and Consolidated Particle Packing and Coating Strength. *J. Pulp Paper Sci.* **33**(2): 71–78, 2007.
8. G.M. Laudone, G.P. Matthews and P.A.C. Gane. Modelling the shrinkage in pigmented coatings during drying: A stick-slip mechanism. *J. Colloid Interface Sci.* **304**:180–190, 2006.

9. P.A.C. Gane, M. Salo, J.P. Kettle and C.J. Ridgway. Comparison of Young-Laplace Pore Size and Microscopic Void Area Distributions in Topologically Similar Structures: a new method for characterising connectivity in pigmented coatings. *J. Mater. Sci.* **44**(2):422–432 2009.
10. J.E. Mark. **Physical Properties of Polymers Handbook**, American Institute of Physics, Woodbury, New York, 1996.
11. Landolt-Börnstein. **Zahlenwerte und Funktionen**. Band IV Technik, 4. Wärmetechnik a, 6. Auflage, Heidelberg, 1980.
12. Landolt-Börnstein. **Zahlenwerte und Funktionen**. Band IV Technik, 4. Wärmetechnik b, 6. Auflage, Heidelberg, 1980.
13. C.J. Ridgway, P.A.C. Gane and J. Schölkopf. Modified Calcium Carbonate Coatings With Rapid Absorption and Extensive Liquid Uptake Capacity. *Colloids and Surfaces A*. **236**(1–3): 91–102, 2004.
14. P.A.C. Gane, C.J. Ridgway, J. Schölkopf and D.W. Bousfield. Heat Transfer through Calcium Carbonate-based Coating Structures: Observation and Model for a Thermal Fusing Process. *International Printing and Graphic Arts Conference*, Cincinnati, Tappi Press, Atlanta, 2006.
15. P. Gerstner, J. Paltakari and P.A.C. Gane. A Method for the Measurement of Thermal Contact Diffusivity of Paper Coating Structures”, *Nord. Pulp Paper Res. J.* **23**(4):354–362, 2008.
16. P.A.C. Gane, J.P. Kettle, G.P. Matthews and C.J. Ridgway. Void space structure of compressible polymer spheres and consolidated calcium carbonate paper-coating formulations. *Industrial and Engineering Chemistry Research*, **35**(5):1753–1764, 1996.
17. D. Vidal, X. Zou and T. Uesaka. Modeling coating structure development using a Monte Carlo deposition method. Part 1: modeling methodology. *Tappi J.* **2**(4):3–8, 2003.
18. P. Gerstner, J. Paltakari and P.A.C. Gane. A Lumped Parameter Model for Thermal Conductivity of Paper Coatings. *Transp. Porous Med.*, **78**(1):1–9, 2009
19. C.T. Hsu, P. Cheng and K.W. Wong. A Lumped-Parameter Model for Stagnant Thermal Conductivity of Spatially Periodic Porous Media, *J. Heat Transfer*. **117**(2):264–269, 1995.
20. T. Pöhler, K. Juvonen and A. Sneek. Coating Layer Microstructure and Location of Binder – Results from SEM Analysis. *Tappi 2006 Advanced Coating Fundamentals Symposium*, pp. 89–100, Turku, Finland, Tappi Press, Atlanta, 2006.
21. J.N. Kapur, P.K. Sahoo and A.K.C. Wong. A new method for gray-level picture thresholding using the entropy of the histogram. *Comput. Vision Graphics Image Process.* **29**:273–285, 1985.

## APPENDIX

### Log-normal distribution and error function

For generation of particle sizes in the simulations of particle deposition, the particle size distributions are chosen to follow a log-normal distribution. The

log-normal distribution is a probability distribution of a variable whose logarithm is normally distributed. If  $X$  is a random variable with a normal distribution, then  $Y = e^X$  has a log-normal distribution. Or in return, if  $Y$  is log-normally distributed, then  $\ln(Y)$  is normally distributed.

A log-normal distribution is, therefore, an analogue to the probability density function of a normal distribution,

$$p_{\text{normal}}(X) = \frac{1}{\tau_{\text{normal}} \sqrt{2\pi}} e^{-\frac{(X - \nu_{\text{normal}})^2}{2\tau_{\text{normal}}^2}} \quad (\text{A1})$$

where  $\nu_{\text{normal}}$  and  $\tau_{\text{normal}}$  are the mean and standard deviation, respectively, such that the probability density function for the particle size  $d$  of a log-normal distribution is defined as:

$$d \cdot p_{\text{log-normal}}(d) = \frac{1}{\tau_{\text{log-normal}} \sqrt{2\pi}} e^{-\frac{(\ln(d) - \nu_{\text{log-normal}})^2}{2\tau_{\text{log-normal}}^2}} \quad (\text{A2})$$

where  $\nu_{\text{log-normal}}$  is the mean and  $\tau_{\text{log-normal}}$  the standard deviation of the variable's natural logarithm. Figure A1.a shows the probability density function of the log-normal distribution having the parameters  $\nu_{\text{log-normal}} = 0.47000$  and  $\tau_{\text{log-normal}} = 0.89231$  (used to describe bcGCC). Note that the curves shown in the following figures are based on weight percent. For generation of particle systems in the simulations, the distribution functions were converted to a particle number based form.

Integration of equation 2 delivers the cumulative distribution function, shown in Figure A1.b:

$$P_{\text{log-normal}}(d) = \frac{1}{2} + \frac{1}{2} \operatorname{erf} \left[ \frac{\ln(d) - \nu_{\text{log-normal}}}{\sqrt{2}\tau_{\text{log-normal}}} \right] \quad (\text{A3})$$

for which  $\operatorname{erf}(x)$  is the Gauss error function, defined as:

$$\operatorname{erf}(x) = \frac{2}{\sqrt{\pi}} \int_0^x e^{-t^2} dt \quad (\text{A4})$$

### **Fitting of the particle size distribution**

The fitting of the log-normal distribution to the particle size distribution measured by the Sedigraph method, was done using the two points of the

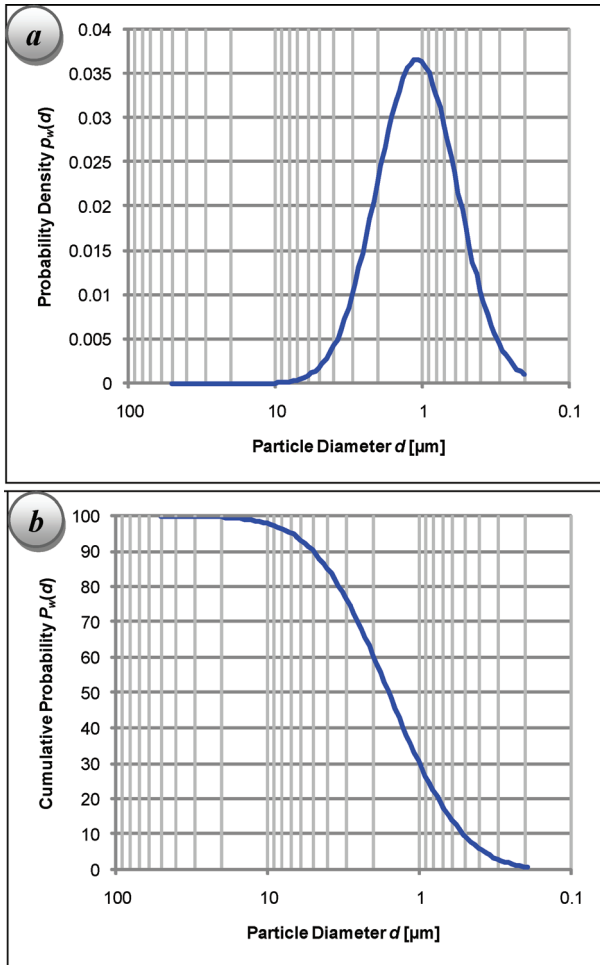


**Figure A1.** a) Probability density function,  $p_w(d)$ , of the log-normal distribution for  $v_{\log\text{-normal}} = 0.47000$  and  $\tau_{\log\text{-normal}} = 0.89231$ . b) shows the corresponding cumulative probability function.

mean particle size ( $d_{50}$  – the weight median particle size, i.e. the size at which 50 wt% of the material is finer) and the top cut ( $d_{98}$  – the size at which 98 wt% of the material is finer). A comparison of the experimentally measured particle size distribution and the current fit is given in Figure A2. It shows that the fitting using median and top cut, results in a good fit for particles larger

than 2  $\mu\text{m}$ . However, for smaller particle sizes the fitting underestimates the weight percentage, i.e., the gap of the log-normal curve to the Sedigraph measurement curve widens. Nonetheless, for reasons of computational

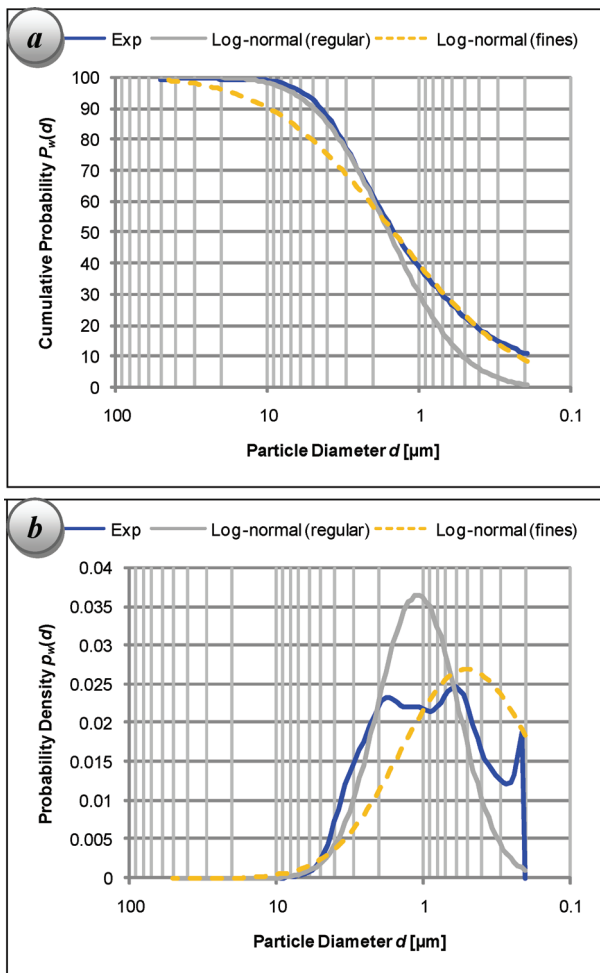


**Figure A2.** a) Sedigraph data of the bcGCC (Exp) compared to the log-normal cumulative weight,  $w$ , distribution,  $P_w(d)$ , based on top cut ( $v_{\log\text{-normal}} = 0.47000$  and  $\tau_{\log\text{-normal}} = 0.89231$ ) and the log-normal cumulative distribution fitted to the fines fraction ( $v_{\log\text{-normal}} = 0.397662$  and  $\tau_{\log\text{-normal}} = 1.48027$ ) b) shows the corresponding probability density functions,  $p_w(d)$ .

tractability, as we go on to elucidate, this distribution has been chosen for the simulations.

Alternatively, one can make a second fitting of a log-normal distribution to only the measurement data finer than 2  $\mu\text{m}$ . This results in a better approximation of fines, but in a considerably worse replication of coarser particles. Theoretically, a weighted combination between both fittings would be possible. However, the very large number a fine particles requires further consideration.

When using the parameters of the fines fitting ( $v_{\text{log-normal}} = 0.397662$ ,  $\tau_{\text{log-normal}} = 1.48027$ ) to generate a particle system for simulation, this results in a computationally unreasonable large number of particles. Compared to the particle system of the coarse particle fit, containing a number ca. 1 000 to 2 000 particles (see domain data in the main article), the fines fit particle system contains ca. 300 000 particles. Since the calculation demand of particle overlapping increases with approximately  $2^N$  for  $N$  particles, and the demand of the statistical particle deposition algorithm is increasing as well, it leads to unfeasible calculation times for today's PC systems, and is even laborious for super or cluster computing solutions (compare ref. [17]).

In addition to the computational reasons for choosing the coarse particle fitting size distributions, there are further geometrical considerations. In two dimensional packing simulations the difference to real three dimensional systems, in which additional interactional forces are also present, is likely to be large in itself, irrespective of the goodness of fit for the particle size distribution. This holds particularly true for the simulations in this study, because of the absence of any surface chemical forces in the simulations. For simulating the surface chemical forces, the fines become increasingly important because of their large specific surface.

## Transcription of Discussion

# A STRUCTURAL ANALYSIS OF THE THERMAL CONDUCTIVITY OF PAPER COATINGS: APPLICATION OF PARTICLE DEPOSITION SIMULATION TO A LUMPED PARAMETER MODEL

*Philip Gerstner*,<sup>1</sup> *Cathy J. Ridgway*,<sup>2</sup> *Jouni Paltakari*<sup>1</sup>  
and *Patrick A.C. Gane*<sup>1,2</sup>

<sup>1</sup>Helsinki University of Technology, Faculty of Chemistry and Materials  
Science, Department of Forest Products Technology, Vuorimiehentie 1A,  
P.O. Box 6300, 02150 Espoo, Finland

<sup>2</sup>Omya Development AG, CH-4665 Oftringen, Switzerland

*Bill Sampson* University of Manchester (from the chair)

You have done this particle deposition, and so you effectively have Monte Carlo simulation and then you split that up to do the lumped parameter model. Have you looked at how different random seeds in that particle deposition affect the outcome of your simulation?

*Philip Gerstner*

Random seeds?

*Bill Sampson*

You make one structure by settling down the particles in a stochastic way, but if you do it again you will get a different structure. How characteristic is that structure?

*Discussion*

*Philip Gerstner*

Of course, we did a number of those simulations and used the mean values for that and I have also plotted the standard deviation.

*Bill Sampson*

So the question is, how many do you need to get that standard deviation to narrow?

*Philip Gerstner*

We made four simulations to do that and that seemed sufficient. I should add perhaps that, when it comes to those simulations that we made them on regular office PCs. So one simulation took about 4 hours to conduct, and I rented a computer classroom where I did those on every computer just to get repeatability.

*Ilya Vadeiko*      FPIInnovations

Could you go back to the slide where you showed experimental data for thermal conductivity with increasing binder content (figure 12a in the paper in the proceedings, ed.)? In the experimental data you see two trends: first an increase and then a decrease, but your model results show monotonic increase. So I was wondering if you have any idea what could be responsible for changes in the behavior of the conductivity in the real system, in real coating?

*Philip Gerstner*

Yes, that is a colloidal force, we think, which effectively rejects the binder particles from the bulk water phase, and drives them to the pigment nodal points. That results in pigment disruption and this is already the case for quite low concentrations of binder. At the same time, you also get an improvement in connectivity that the binder creates at the pigment nodal points. But this improvement in connectivity is overlapped with the pigment disruption, and therefore you get a maximum.

*Ilya Vadeiko*

So, after introducing two new parameters for connectivity, were you able to reproduce this maximum?

*Philip Gerstner*

Only one factor has been introduced – it is the pigment connectivity. By adding that we can fit the experimental data to the model and as a result we get the newly introduced factor of pigment connectivity. We have seen that the pigment connectivity is reduced initially when adding binder. This was seen on the last slide (figure 19 in the paper in the proceedings, ed.).

*Ramin Farnood*      University of Toronto

This is just a comment. We have done a 3D simulation, to follow up on your equation, and we are able to predict precisely not just the trend, but also the values using only the pigment and binder thermal conductivity values.

*Tetsu Uesaka*      FPIInnovations

This is also another comment. I wonder why you have to use this so-called lumped parameter method because, obviously, this method does not consider geometries, randomness and length scales. On the other hand, in this specific system, there is an approximate (but quite accurate) analytical solution obtained by Torquato based on multipoint correlation functions. Since you already have all the spatial information from either the simulation or the experiment, you can almost automatically determine these correlation functions at the different orders. So it is an almost perfect opportunity to compare that model as well as a smeared-out model too.

*Philip Gerstner*

Yes. I accept the comment, but we also think that this lumped parameter model in its simplicity is a very nice way to illustrate the coating structure in terms of porosity and connectivity, because it is reflected in this unit cell approach.